

NJC

Facet-dependent adsorption of safranin dye and phosphate ions by synthesized hematite nano-rods derived from natural Lateritic iron ore; steric and energetic investigation

Journal:	New Journal of Chemistry		
Manuscript ID	NJ-ART-09-2024-004152.R1		
Article Type:	Paper		
Date Submitted by the Author:	1 16-0CT-7074		
Complete List of Authors:	Mostafa, Dina; Beni-Suef University, Environmental Science and Industrial Development Department Shehata, Nabila; Beni-Suef University, Environmental Science and Industrial Development Department; Beni-Suef University, Renewable Energy Science and Engineering Department Shaban, Mohamed; Islamic University of Madinah, Department of Physics Alqhtani, Haifa; Princess Nourah bint Abdulrahman University, Biology Allam, Ahmed; Imam Muhammad Ibn Saud Islamic University, Department of Biology; Beni Suef University, Department of Zoology Abukhadra, Mostafa; Beni Suef University Faculty of Science,		

SCHOLARONE™ Manuscripts

Facet-dependent adsorption of safranin dye and phosphate ions by synthesized hematite nano-rods derived from natural Lateritic iron ore: steric and energetic investigation

Dina Mostafa¹, Nabila Shehata^{1,2}, Mohamed Shaban⁸, Haifa A, Alghtani⁴, Ahmed A, Allam^{5, 6}; Mostafa R, Abukhadra⁸

1 Environmental Science and Industrial Development Department, Faculty of Postgraduate Studies for Advanced Sciences, Beni-Suef University, Beni-Suef, Egypt *Renewable Energy Science and Industrial Development Department, Faculty of Postgraduate Studies for Advanced Sciences, Beni-Suef University, Beni-Suef, Egypt

*Renewable Energy Science and Engineering Department, Faculty of Postgraduate Studies for Advanced Sciences, Beni-Suef University, Beni-Suef, 62511, Egypt

*Department of Physics, Faculty of Science, Islamic University of Madinah 42351, Saudi Arabia

*Department of Biology, College of Science, Princess Nourah bint Abdulrahman University, P.O. BOX 84428, Riyadh 11671, Saudi Arabia

*Department of Biology, College of Science, Imam Mohammad Ibn Saud Islamic University, Riyadh 11623, Saudi Arabia

Department of Zoology, Faculty of Science, Beni-suef University, Beni-suef 65211 Egypt.

Materials Technologies and their Applications Lab, Geology Department, Faculty of Science, Beni-Suef University, Beni suef City, Egypt.

Corresponding author Email*: Abukhadra89@Science.bsu.edu.eg (M.R.A.),

Abstract:

Natural lateritic iron was subjected to a morphological transformation process based on a simple alkaline hydrothermal treatment process, producing well-developed hematite nanorods (HM24). The rods display mesoporous properties (4.2 nm average pore diameter) and significant surface area (141.5 m²/g). The developed nanorods were applied as enhanced adsorbents for phosphate ions (PO₄³⁻) and safranin dye (SFR) considering the changes in the exposed crystalline face. The recognized results revealed that the modified form with its nanorod morphology and different exposed face (012) displays better uptake performance for both PO₄³⁻ (148 mg/g) and SFR (211.4 mg/g) than the raw sample and numerous investigated adsorbents in the literature. This was reported considering the experimental conditions at (pH: 5 for PO₄³- and 8 for SFR; a temperature: 30 °C; volume: 100 mL; concentration: 350 mg/L; duration: 24 h; and dose: 0.4 g/L). The advanced isotherm assessments, based on the derived monolayer model and statistical physics concepts, reveal the enrichment of the rods with active site densities of approximately 84.8 mg/g for SFR and 38.8 mg/g for PO₄³. Each of these sites can be filled with 3 molecules of SFR and 5 ions of PO₄³, suggesting multi-ionic interactions and vertical configurations of these adsorbed pollutants. The energetic investigations (less than 40 kJ/mol) suggest that the active sites of HM24 uptake both SFR and PO₄3- through various physical mechanisms. This might include electrostatic attractions, hydrogen bonds, and van der Waals forces. These mechanisms exhibit spontaneous and exothermic properties considering the findings of the thermodynamic functions (enthalpy, entropy, and internal energy). The structure also exhibit marked recyclability to be reused six times with significant capacity.

Keywords: Laterite, hematite, nano-rods, adsorption, pollutants, advanced equilibrium

Introduction:

The main concern facing contemporary society is the pollution of potable water and the safety of its populations [1, 2]. The World Health Organization (WHO) has issued a serious warning, projecting severe water shortages for more than 50% of the global population by 2025 [2, 3]. Industrial, agricultural, and mining operations release a wide range of water pollutants, including bacteria, herbicides, hazardous metals, toxic fertilizers, pharmaceutical residuals, and dyes [4, 5]. The release of the industrial and agricultural effluents that are enriched in soluble phosphate ions (PO₄³) into the water supplies, specifically closed lakes, at concentrations higher than 0.05 mg/L seriously affects the quality of the water and aquatic environments. The uncontrolled and random discharge of phosphate as a water pollutant facilitates the uncontrolled growth of phytoplankton and algae, leading to the emergence of eutrophication [8, 9]. Furthermore, the wide application of synthetic dyes in numerous sectors such as textiles, paper, plastics, and leather as vital pigments is associated with extensive release of such organic compounds into the aquatic ecosystem [10, 11]. Annually, an estimated 700,000 tons of such dyes are projected to be released into the surrounding rivers and aquatic ecosystems [12]. A significant number of marketed dyes are highly toxic and very resistant to biodegradation, leading to adverse impacts on ecosystems and human health [3, 12]. Safranin (SFR) is a water-soluble basic azine dye that is widely used for printing textiles, staining, microbiological verification, medication, and food packaging [13, 14]. The complex structure and durability of SFR represent the main challenge and difficulty during its biological decomposition [14]. The organic structure of the dye exhibits a destructive effect on the nucleic acid that exists in bacteria in addition to its carcinogenic properties. Prolonged or short-term exposure of human beings to SFR may result in numerous adverse health effects, including irritation of the eyes, lips, tongue, and stomach, as well as nausea, emesis, and gastrointestinal distress [13, 15].

Numerous studies have established that advanced oxidization, ozonation, flocculation, adsorption, nanofiltration, membrane separation, biological decomposition, ion exchange, and coagulation are effective techniques for removing many types of contaminants [1, 7, 16]. Blocked membranes may impede the functioning of filtration systems by effectively plugging their interior pores. This results in an increase in the required pressure and energy consumption, significantly shortens the membranes' lifespan, and significantly increases the cost of the technique. Nevertheless, it is advisable to employ adsorption methods in order to minimize the detrimental impacts of the resultant chemical byproducts throughout the oxidization and catalytic decomposition activities [17, 18]. A number of investigations have demonstrated that adsorption by novel materials is an affordable, effective, reliable, effortlessly, readily available, and reusable method for eliminating diverse species of water contaminants [19, 20]. Several factors, including production costs, fabrication procedures, precursor availability, adsorption efficiency, recyclability, retention velocity, sustainability, uptake specificity, safety, and reactivity, influence the selection of a suitable absorbing material [21, 22]. Therefore, researchers have conducted a thorough evaluation to produce novel adsorbents using easily accessible and economically feasible constituents frequently encountered in Earth's resources [1, 23, 24]. The use of well-

established adsorbents obtained from earth's resources, such as various minerals and rocks, is strongly recommended due to their significant environmental and economic benefits [25].

Iron oxide nanoparticles possess a distinctive set of qualities that distinguish them from various nanomaterials [26]. These qualities include their high reactivity, visible light absorption efficiency, adsorption performance, chemical and mechanical stability, biological compatibility, and surface area, in addition to the affordable prices and significant abundance within the Earth's resources. Furthermore, they demonstrate remarkable magnetic properties, excellent conductivity, and facilitate easy separation and recovery [26, 27, 28]. Such properties demonstrated their applicability in a number of applications, including fertilizers, anti-virus agents, adsorption and advanced oxidation water purification, as well as soil remediation [27, 29]. Hematite (α-Fe₂O₃) is a highly stable iron oxide derivative that exhibits n-type semiconductor characteristics. Hematite was studied extensively as a functional ingredient for various environmental along with industrial uses, serving as both an adsorption agent and a catalyst [26, 30]. Numerous factors, including production procedures, morphological properties, used precursors, and precipitation reagents, greatly influence the structural, physicochemical, and textural characteristics, as well as the activities of iron oxides [31].

Metal oxide-based nanostructures' morphology and structural configurations significantly influence their chemo-adsorption and catalytic performance, and applying morphological modifications can effectively enhance these technical properties [32]. Previous studies have shown that hematite nanoparticles with controlled and improved shapes, such as nanosheets, nanorods, nanospheres, and cauliflowers, have better physical and chemical properties [30]. 1D nanorods have attracted significant attention because of their uniform geometry, unique structure, and outstanding technical characteristics in a wide range of uses [33, 34]. Regrettably, the majority of the techniques used to produce one-dimensional (1-D) materials include expensive raw materials that are mostly chemicals, surfactants, templates, and high synthesis temperatures. As a result, it is critical to use simple and cost-effective techniques that operate at moderate temperatures, as well as readily available raw materials. The hydrothermal approach has gained considerable attention due to its ability to precisely control the microstructure, morphology, crystallite size, and physiochemical properties of materials at the nanoscale [33, 35]. Moreover, the reactive nature of hematite nanostructures exhibits significant facet dependency, which is intricately linked to the markedly different ionic configurations, resulting in varied Fe-O binding topologies, active site quantities, and surface charge characteristics [26, 36].

Therefore, the presented study here involved the synthesis of well-developed hematite nanorods from natural iron raw material as geological lateritic iron ore through facile alkaline hydrothermal treatment steps at

mild temperature conditions as low cost and a naturally based structure of high natural availability. The obtained hematite nanorods were assessed as potential adsorbents for inorganic phosphate ions (PO_4^{3-}) and organic synthetic safranin dye (SFR) from the water resources and the aquatic environment. The adsorption properties and mechanism were monitored based on the effect of the essential experimental factors, common kinetic models, classic isotherm studies, and other equilibrium models derived from the statistical physics theory and the corresponding steric and energetic parameters.

2. Experimental Work

2.1. Materials

Natural iron precursor was delivered as lateritic iron ore from El-Gedida area, Bahariya Oasis, Western Desert, Egypt. The sample chemically composed of 96.73% Fe₂O₃ as the main content in addition to other impurities represented essentially by 1.64% SiO₂ and 0.72% Al₂O₃. NaOH with a purity of over 98% was purchased from Sigma-Aldrich in Egypt. The adsorption experiments involved safranin-O synthetic dye (\geq 85%; Sigma-Aldrich), together with phosphate standard solution (1000 mg/L; Sigma-Aldrich) as the primary sources of the polluted solutions.

2.2. Synthesis of hematite nano-rods

The raw iron ore was crushed and ground by ball mill for 4 h obtaining fine powder with size range from 25 to 60 µm. Certain weight of the ground product (15 g) was pulverized within alkaline solution of NaOH (100 mL; 0.4 M) under continuous stirring for 2 h at room temperature. After that, the mixture was transferred into hydrothermal synthesis reactor of Teflon lined stainless steel autoclave and then treated thermally for 24 hours at 100 °C using electrical and digital muffle furnace with temperature elevation rate 5 °C per minute. After this stage, the autoclave was cool down to the room temperature and the hydrothermally treated particles were extracted by centrifugation for 15 min at rotation speed of 300 rpm. Then, the product was washed, rinsed, and dried for 5 h at 80 °C. The dried product was labeled as HM24 and kept for the further characterization and applications steps.

2.3. Characterization instruments

The mineral phases and crystallographic properties were examined and explored by utilizing X-ray diffraction (XRD) patterns produced by the PANalytical-Empyrean X-ray diffractometer. The range of values for the 2 Theta angles determined with the diffractometer is between 0 and 70°. A Fourier transform infrared spectrometer (FTIR-8400S; Shimadzu) that possesses a 400–4000 cm⁻¹ determining range was employed in addition to the energy dispersive X-ray (EDX) investigation of elemental contents to establish the changes in

the functioning chemical groups across the production processes. The exterior properties of the produced structures were studied by applying a Gemini Zeiss Ultra 55 scanning electron microscope. Before examination, the outer surfaces of the products under exploration had been coated with a thin film of gold through the spraying process. The porosity of HM24 along with the exact surface area have been determined employing a surface area analyzer (Beckman Coulter SA3100) after expelling any gases out of the material being examined. The measurements were successfully accomplished by employing the conventional isotherms for N_2 adsorption and desorption.

2.4. Adsorption studies

Experimental adsorption studies of PO₄³⁻ as well as SFR were conducted in batches. The experimental parameters that were evaluated were the following: pH (pH 2–8), time span of the reaction (15–1440 min), amount of HM24 (0.4 g/L), and dissolved contents of the tested pollutants (50–350 mg/L) under three different operational temperature values (30 °C, 40 °C, and 50 °C) and particular volumes (100 mL). Three rounds were conducted for each test, and the averages of the obtained findings were consistently used in the calculations, with standard deviations below 3.4% (PO₄³⁻) and 4.9% (SFR). The achieved uptake capacities (Qe) of both SFR and PO₄³⁻ were calculated employing Equation 1. The remaining PO₄³⁻ ions were quantitatively determined using the Dionex DX-120 ion chromatography instrument. The remaining contents of SFR were quantified employing a UV-Vis spectrophotometer using a detecting wavelength of 521 nm.

$$Q_e (mg/g) = \frac{(C_o - C_e)V}{m}$$
 (1)

2.5. Conventional and modern equilibrium investigations

The adsorption of SFR and PO_4^{3-} using HM24 has been described using well-established traditional kinetics, classic equilibrium, and updated isotherm investigations in accordance with the theoretical statistical physics hypothesis (Table S1). The kinetic and conventional isotherm modeling have been assessed employing the non-linear fitting levels of the retention data of SFR and PO_4^{3-} . The evaluation implemented the parameters of the coefficient (R2) (Eq. 2) and Chi-squared (χ^2) (Eq. 3). The nonlinear fitting qualities with the modern isotherm models' descriptive equations and the remediation results of SFR and PO_4^{3-} have been examined using the determination coefficient (R2) and root mean square error (RMSE) (Eq. 4). The variables m', p, Qe_{cal} , and Qe_{exp} in the equation correspond to the outcomes of SFR and PO_4^{3-} sequestration, parameters affecting the sequestration reaction, predicted capacities of ions sequestration, and determined capacities of ions sequestration, respectively.

$$R^{2} = 1 - \frac{\sum (Q_{e, exp} - Q_{e, cal})^{2}}{\sum (Q_{e, exp} - Q_{e, mean})^{2}}$$
(2)

§4

$$\chi^{2} = \sum \frac{(Q_{e, exp} - Q_{e, cal})^{2}}{Q_{e, cal}}$$
 (3)

RMSE =
$$\sqrt{\frac{\sum_{i=1}^{m} (Qe_{cal} - Qe_{exp})^2}{m' - p}}$$
 (4)

3. Results and discussion

3.1. Characterization of the adsorbent

The structural properties of both raw iron oxide and the modified version were assessed based on their XRD patterns (Fig.1). The obtained pattern of raw samples reveals its nature as α-hematite with typical rhombohedral crystal lattice (JCPS Cd. No. 33-0664; ICDD No. 01-079-0007). The identification diffraction peaks were identified at 24.5° (012), 33.5° (104), 35.9° (110), 41.2° (113), 49.7° (024), 54.5° (116), 62.7° (214), and 64.3° (300) (Fig.1A) (JCPS Cd. No. 33-0664). After the modification step, the obtained patterns demonstrate no changes in the identified hematite phase but exhibit remarkable indications about its impact on the structure properties of the sample (Fig.1B). The peaks displayed observable reduction in their intensities and sometimes some peaks can be hardly detected in addition to remarkable deviation to lower positions. The main peaks were deviated to 24.05°, 33.17°, 35.6°, 40.8°, 49.3°, 54.2°, 62.3°, and 63.8° demonstrating either reduction in the crystallite size or lattice deformation (Fig.1B). Nevertheless, hematite crystals with completely different exposed facets exhibit changes in their peak strengths. The presented patterns show noticeable reduction in the intensities of (110) and (104), the main peaks, in the modified form of HM24 compared to the original sample. These observations indicate that the modified crystals have different exposed faces [26, 36]. Also, the determined average crystallite size demonstrates such structural impact as the size reduced from 18 nm for raw sample to 13.3 nm for HM24.

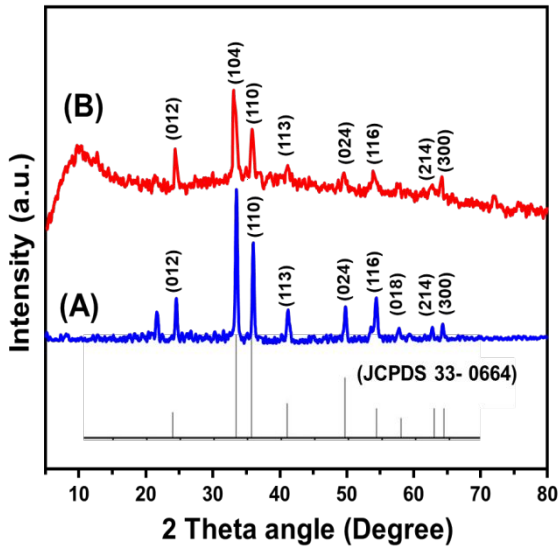


Fig.1. XRD patterns of raw lateritic iron ore (A) and prepared hematite by alkaline modification (HM24) (B)

The inspected FT-IR spectra also reveal considerable indications about the structural changes during the alkaline modification of natural iron ore (Fig.2). The spectrum of raw ore shows no indications about the

52

⊉9

OH groups either those corresponding to adsorbed water molecules or the structural OH of iron hydroxide forms. The marked bands around 428 cm⁻¹ (Fe-O-Fe) and 525 cm⁻¹ (Fe-O) revealed the existence of the hematite phase (Fe₂O₃) (Fig.2A) [37, 38]. The marked band at about 889 cm⁻¹ (Fe-O) might give indications about the existence of goethite mineral [39]. The detectable bands around 798 cm⁻¹ and 1005 cm⁻¹ signified the Si(Al)–O groups which are corresponding to the existed silicate or clay impurities (Fig.2A) [37, 40]. The impact of the alkaline modification process appeared significantly in the inspected FT-IR spectrum of HM24. The spectrum declared the existence of numerous new bands corresponding to the hydroxyl groups (3399 cm⁻¹, 3097 cm⁻¹, and 1640 cm⁻¹) (Fig.2B) [39]. This demonstrating the hydration effect of the modification reactions and changes in then exposed crystal facets. Moreover, the corresponding bands of the iron bearing chemical groups showed remarkable increment in their intensities as well as their broadness and considerable shift from their original positions. The identification bands of hematite were deviated to 436 cm⁻¹ (Fe-O-Fe) and 553 cm⁻¹ (Fe-O) (Fig. 2B). This declared the structural impact of the modification process on the crystal structure of hematite.

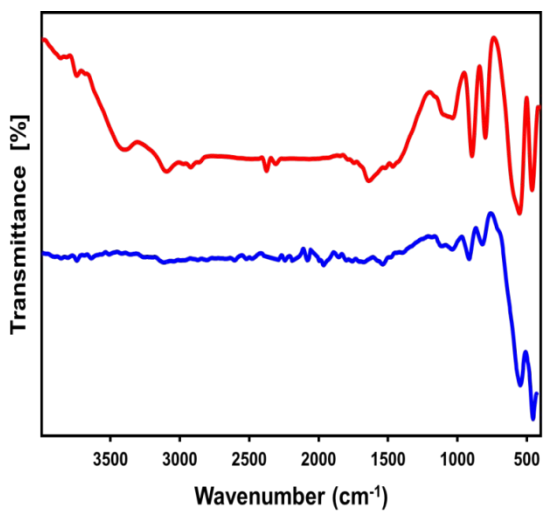


Fig.2. FT-IR spectra of raw lateritic iron ore (A) HM24 particles (B)

The modification step also affected significantly the morphological features of the hematite grains (Fig.3). The SEM images of the inspected hematite grains within the used lateritic iron ore appeared as massive and agglomerated particle sometimes appeared with irregular topography (Fig.3A). This irregular topography can be described as coating layer of nano-grains possesses flakey, longitudinal, and elliptical shapes (Fig.3B). By conducting the alkaline modification step, the SEM images of HM24 revealed the significant morphological transformation of the modified hematite into well-developed nano-rods with estimated length range from 100 nm to 250 nm and diameter range from 10 nm to 50 nm (Fig.3C and D). Such morphological feature can significantly impact the surface area, reactivity, and exposed active sites and in turns the adsorption performance of hematite.

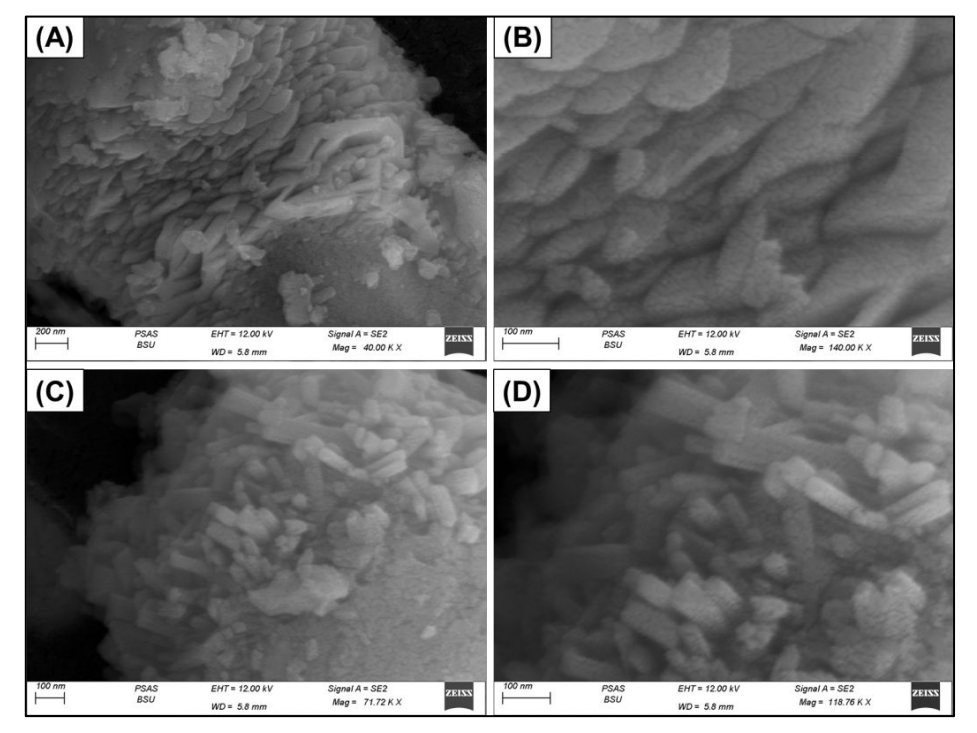


Fig.3. SEM images of raw iron ore (A and B) and synthetic HM24 grains (C and D)

Texturally, the properties of synthesized HM24 particles were evaluated based on their nitrogen adsorptiopn/desorption isotherm curve (Fig. 4). The curve can be classified as a type IV isotherm according to the basics of the International Union of Pure and Applied Chemistry (IUPAC). Additionally, the curve exhibits a noticeable hysteresis loop of type H3 from $P/P_0 = 0.50$ to 1 [41]. Such criteria reflect the existence of the mesoporous structure of HM24, which can be assigned to the non-rigid aggregation or slit-shaped pores [41]. The size distribution curve reflected the formation of the pores, with sizes ranging from 1.7 nm up to 9.2 nm, and the majority of pore diameter concentrates around 3.4 nm, while the average pore diameter is 4.5 nm (Fig. 4). Regarding the measured specific area, the synthetic HM24 possesses an execllent value equal to 141.5 m^2/g . This qualifies the synthetic strucrure to be applied effectively, either as an adsorbent for water contaminants or as a heterogeneous catalyst, in addition to other applications as a drug delivery system or as catalyst support, considering its porosity and significant surface area.

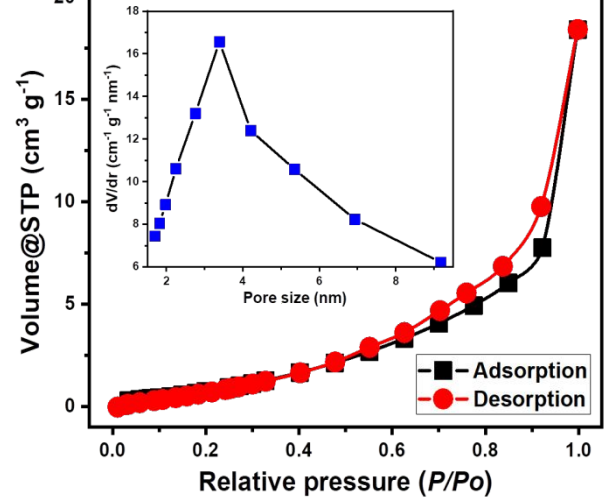


Fig.4. The nitrogen adsorption/desorption isotherm curve and pore size distribution properties of HM24

24/5

246

8

55

97

53

2<u>5</u>4

57

8

59

2ể⊈

262

63

63

69 36

77

272

3.2. Adsorption results

3.2.1. Effect of pH

The pH of the water-based solution under study strongly influences the main surface charges and ionization properties of the dissolved chemical compounds [16]. The experimental pH effect was monitored over a variety of pH values spanning between 2 and 8. The remaining variables were maintained at precise levels: a reaction duration of 120 minutes, a temperature of about 30 °C, a studied volume of 100 mL, a contaminants level of 100 mg/L, and a HM24 dose of 0.4 g/L. The adsorption analysis for SFR shows a notable increase as greater pH values are examined, attaining a pH of 8 (83.4 mg/g) (Fig.5). Across the pH range that was investigated, the water-soluble SFR dye was detected and classified as cationic molecules. Furthermore, the predicted deprotonation of the functional groups distributed throughout the surface of HM24 under more basic conditions leads to the entire saturation of the outermost layer in hydroxyl ions that carry negative charges. Therefore, the high pH conditions offer a favorable setting for strong electrostatic attractive forces to occur in place between the water-soluble contaminants (SFR) and the exterior surface of HM24 [20, 42, 43].

Depending on the adjusted pH, phosphate ion adsorption displays different behaviors. The greatest elimination value was detected at a pH of 5, with a binding effectiveness of 44.9 mg/g. Nevertheless, the efficacy of HM24 diminished above pH 5 until pH 8 (Fig. 5). Investigation of the ionization properties of watersoluble phosphate considering different pH limitations reflected significant changes. Under acidic conditions with a pH of less than 3, phosphate was categorized as a neutral variety (H₃PO₄). At pH values ranging from 3 to 6, it was present in its acidic H₂PO₄- form. Under conditions of neutrality and alkalinity, when the pH exceeds 6, phosphate exists in two more acidic forms, namely HPO₄2- and PO₄3- [7, 44]. Under acidic conditions, HM24 exhibited limited uptake efficacy according to its ionization tendencies of phosphate and protonation/deprotonation features of hematite within the evaluated pH values. The reason for this phenomenon may be attributed to the hydrogenated outermost surface of HM24, which displays a low electrostatic attraction for the neutral phosphate (H₃PO₄). As the pH rose, the electrostatic attraction forces progressively intensified, resulting in enhanced uptake for the dominant acidic phosphate forms (H₂PO₄-) inside the solution under such a pH range. The consequence was a notable augmentation in the recognized effectiveness of HM24 up to a pH of 5. Moreover, the deprotonation of HM24 at pH values higher than pH 5 resulted in an abundance of chemical groups with net negative charges. These groups possess notable repulsive properties towards previously established phosphate forms, specifically HPO₄²⁻ and PO₄³⁻ [8, 45].

Measurements of the pH level at the zero point charges (pH_(pzc)) have supported the prior findings. The measured values of pH _(pzc) following PO₄³⁻ and SFR uptake were 7.6 and 6.2, respectively. Above these boundaries, the surficial charges are mostly negative, resulting in SFR's electrostatic attraction. Furthermore, at pH levels lower than these thresholds, the exterior charges across the adsorbent tend to be positive, which promotes PO₄³⁻ ions uptake [46, 47, 48].

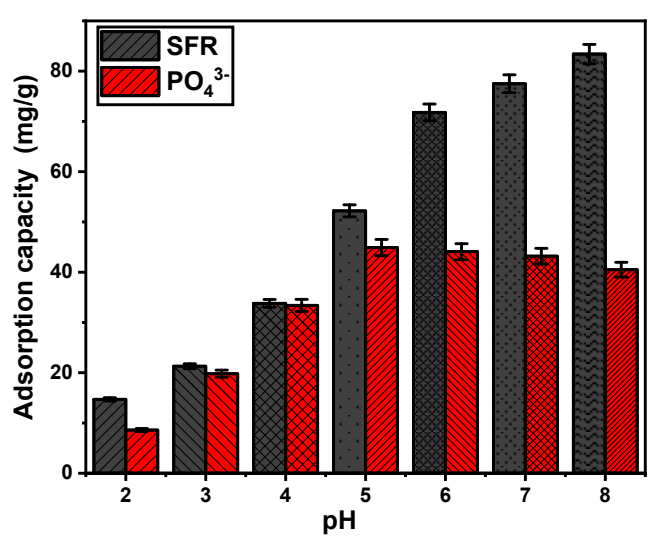


Fig.5. The experimental effect of the solutions pH on the uptake behaviors of SFR and PO₄³⁻ by HM24 (duration: 120 minutes; a temperature: 30 °C; volume: 100 mL; concentration: 100 mg/L; and dose: 0.4 g/L)

3.2.2. Contact time

An analysis was conducted to assess the adsorption characteristics of HM24 with regard to the efficacy of eliminating PO₄³⁻ and SFR. The examination encompasses a testing range from 14 to 1440 minutes. After verifying the levels of essential parameters, including the level of contaminants (100 mg/L), temperature (30 °C), volume (100 mL), pH (5 for PO₄³⁻ and 8 for SFR), and quantity (0.4 g/L) at fixed values, we evaluated the specific impact of distinct time periods. All over the experiments, the effectiveness of HM24 in removing PO₄³⁻ and SFR showed a significant increase in both the quantity of ions adsorbed and their experimental uptake rates. Moreover, it is crucial to acknowledge that the time frame of the experiments significantly influences the detectable enhancements in the recognized uptake properties, attaining about 480 minutes (Fig. 6A). Nevertheless, there were no notable changes or improvements seen in the rate of elimination of PO₄³⁻ and SFR ions or the amount of these ions adsorbed after the stated contact durations. Previous findings suggest that HM24 can serve as an adsorbent for PO₄³⁻ and SFR, reaching its maximum stability after a specific duration of 480 minutes. Under such equilibration conditions, the adsorption qualities of HM24 for PO₄³⁻ and SFR were measured to be 81.8 mg/g and 121.4 mg/g, respectively (Fig. 6A). In the early phases of the evaluation, substantial improvements in the adsorption rates of SFR and PO₄³⁻ using HM24 adsorbent were observed along with larger amounts of held ions. The detected improvements were ascribed to the extensive

248

<u>2</u>9

30

§≨ **§**2

33

presence of both active and free sites throughout the HM24 surface [49]. With the extension of the examination's time, the number of unoccupied sites decreased significantly. The prolonged adsorption of PO_4^{3-} and SFR, which consumes the previously described sites and reduces the overall number of unoccupied sites, is the primary factor contributing to this response. Consequently, there was a drastic decrease in the rates by which the PO_4^{3-} and SFR ions adsorbed after a certain duration. Furthermore, the use of HM24 resulted in modest enhancement or consistent characteristics in PO_4^{3-} and SFR adsorption, indicating a state of equilibrium. By completely filling all the existing active functional sites and preventing further adsorption of PO_4^{3-} and SFR on its exterior, HM24 identifies its equilibrium phases [50].

3.2.3. Kinetic studies

3.2.3.1. Intra-Particle diffusion behavior

The examination of intra-particle diffusion characteristics may be used to illustrate the mechanistic stages and adsorption characteristics of PO₄3- and SFR employing HM24. Figure 6B displays three distinct sections of the presented curves, each with different slopes. The analyzed curves exhibit spatial displacements relative to their initial positions, indicating the simultaneous presence of multiple adsorption mechanisms in addition to the diffusion mode of PO₄3- and SFR [7, 51]. The processes generally consist of three main phases: (1) interactions between dissolved ions and the unbound uptake sites distributed across the outer surfaces of HM24 (boundary or external adsorption); (2) the layered adsorption processes (internal adsorption) in conjunction with the diffusion properties of the dissolved chemicals; and (3) the influence of equilibrium or saturating situations [52]. The preliminary results of this study indicate that the external uptake mechanisms are the primary mechanisms responsible for the binding of PO₄3- and SFR to the interface of HM24, which were the most significant pathway consistently detected at all stages of the adsorption activities (Fig. 6B). The effectiveness of adsorbing PO₄³⁻ and SFR during this stage relies on the total number of sites situated across the interfaces of HM24 [18]. The efficacy of further layered or internal adsorption methods was immediately confirmed by increasing the duration until all exterior sites were completely occupied (Fig. 6B) [52, 53]. Moreover, this step incorporates the effects of PO₄3- and SFR diffusion mechanisms. After the establishment of equilibrium situations, the last processes of PO₄3- and SFR adsorption via HM24 exert the substantial impact. These findings show that PO₄³⁻ and SFR, successfully adsorbed, occupied all available sites [54, 55]. Molecular and interionic attraction processes expedite the elimination of PO₄3- and SFR throughout this phase [18].

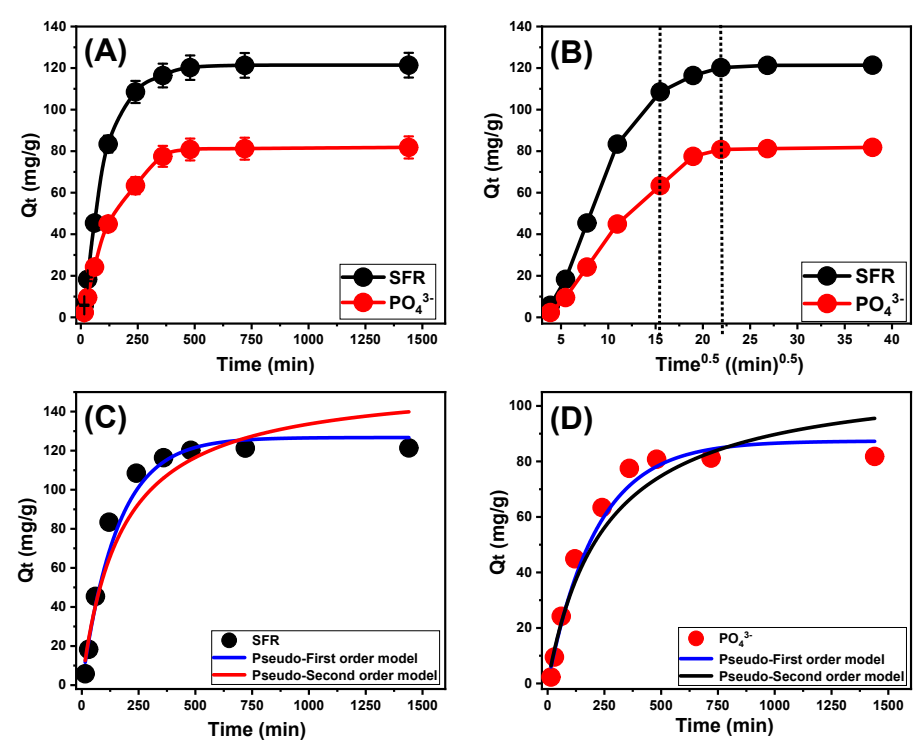


Fig.6. The experimental effect of the contact time on the uptake behaviors of SFR and PO_4^{3-} by HM24 (A), the intra-particle diffusion curves of the adsorption processes (B), fitting of the SFR uptake behaviors with the kinetic models (C), and fitting of the PO_4^{3-} uptake behaviors with the kinetic models (D) (pH: 5 for PO_4^{3-} and 8 for SFR; a temperature: 30 °C; volume: 100 mL; concentration: 100 mg/L; and dose: 0.4 g/L)

3.2.3.2. Kinetic modeling

In order to investigate the time-dependent impacts and comprehend physical mechanisms such as mass transfer pathways as well as chemical-based pathways that regulate absorption efficacy, it is imperative to model the kinetics of the uptake reactions [56]. The kinetics of PO_4^{3-} and SFR removal activities were analyzed employing conventional pseudo-first-order (P.F.) and pseudo-second-order (P.S.) numerical models. The P.F. model was used to elucidate the correlation between the rates at which the PO_4^{3-} and SFR ions completely occupy the interaction binding sites, in addition to their entire quantities. The P.S. principles may highlight the link between the characteristics of analyzed adsorbents across a specific period of time. The correlation between the pollutants adsorption tendencies and the inspected two kinetic models has been assessed by implementing nonlinear fitting variables that correspond to their relevant equations. The best levels of fitting were determined by the analysis of correlation coefficients (R^2) and Chi-squared (X^2) values (Table 1; Figs. 6C and D). The R^2 , in conjunction with the X^2 data, demonstrates that the basic hypotheses of the P.F. model provide a better explanation for the adsorption characteristics of PO_4^{3-} and SFR employing HM24 than the evaluated P.S. concept. The outcomes derived from the numerical simulation of the P.F. model indicated that the predicted quantities of PO_4^{3-} and SFR that can be adsorbed by HM24 are 87.4 mg/g and

89

90 93

95

3<u>5</u>3

3<u>5</u>4

126.7 mg/g, respectively. These values closely matched the experimentally obtained quantities when compared to the P.S. model's results. The established consistency corroborates the previously acquired findings, which emphasize the better suitability of the P.F. hypothesis regarding the kinetic analyses (Table 1). According to P.F. theoretical terms, the main factors contributing to the adsorption of PO₄³⁻ and SFR using HM24 include physical processes, particularly van der Waals forces and electrostatic attractions [57, 58]. The analyzed fitting factors additionally reveal a considerable similarity with the P.S. model; nevertheless, a better degree of match can be achieved utilizing the P.F. model. Previous studies have shown that several chemical mechanisms, including hydrogen bonding, complexation, and hydrophobic interactions, are likely to either enhance or have a negligible impact on the adsorption of PO₄³⁻ and SFR using HM24 [54, 57]. Physical approaches may generate successive uptake layers over the earlier-formed layers of the chemically adsorbed PO₄³⁻ and SFR ions [59].

Table.1. The mathematical parameters of the evaluated kinetic models (pH: 5 for PO₄³⁻ and 8 for SFR; a temperature: 30 °C; volume: 100 mL; concentration: 100 mg/L; and dose: 0.4 g/L)

Kinetic models						
Models	Parameters	SFR	PO ₄ 3-			
	K₁ (min⁻¹)	0.0064	0.0047			
Pseudo-First-order	Qe _(Cal) (mg/g)	126.7	87.4			
	R ²	0.97	0.97			
	X ²	1.6	1.3			
Pseudo-Second-order	k ₂ (g mg ⁻¹ min ⁻¹)	3.72 X 10⁻⁵	3.57 X 10 ⁻⁵			
	Qe _(Cal) (mg/g)	156.6	112.1			
	R ²	0.95	0.95			
	X ²	0.3	2.2			

3.2.4. Starting concentration

The analysis here investigated the impact of initial PO₄³⁻ and SFR concentrations on the maximum elimination activities as measured by HM24, together with the corresponding equilibrium conditions, across the evaluated range from 50 to 350 mg/L. The other essential parameters affecting the elimination of PO₄³⁻ and SFR were maintained fixed at certain values, including a total volume equal to 100 mL, a period of 24 hours, a dose of 0.4 g/L, and temperatures ranging from 303 K to 323 K. A correlation has been found between elevated concentrations of PO₄³⁻ and SFR ions and the detected rise in their adsorbed amounts using HM24 (Fig. 7A and C). Increasing the concentration of PO₄³⁻ and SFR ions in a specific volume significantly improves soluble chemicals' diffusion, driving forces, and mobility properties. This enhancement augmented the ability to interact with larger amounts of the existing active sites that are easily accessible on the exterior of HM24. Therefore, the effectiveness of adsorbing PO₄³⁻ and SFR using HM24 was significantly improved relative to the tested contents of PO₄³⁻ and SFR [60]. Nevertheless, this correlation can only be observed until specific contents of both PO₄³⁻ and SFR. Beyond such concentrations, raising the starting levels of PO₄³⁻ and SFR

doesn't seem to have a positive impact on their binding performances to the interface of HM24. Determining the equilibrium situations facilitates significantly in determining the highest adsorption performances of PO_4^{3-} and SFR by HM24. The highest adsorption capacities of PO_4^{3-} were determined to be 208.5 mg/g at a temperature of 303 K, 182.2 mg/g at 313 K, and 152.6 mg/g at 323 K (Fig. 7A). The measured values for SFR were 146.8 mg/g at 303 K, 125.4 mg/g at 313 K, and 103.8 mg/g at 323 K (Fig. 7B). The observed decrease in the uptake effectiveness of PO_4^{3-} and SFR using HM24 with raising the examined temperatures suggests that the reactions under investigation possess exothermic characteristics.

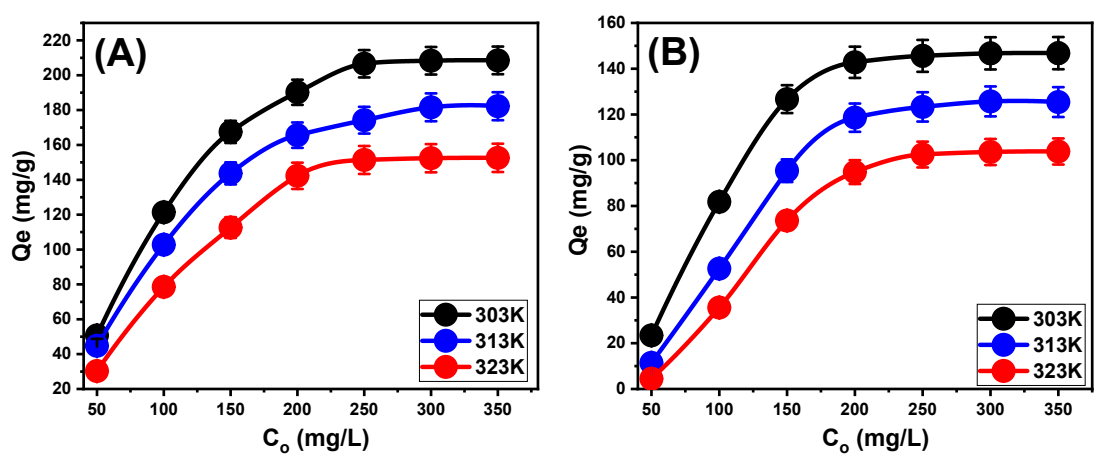


Fig.7. the experimental effect of the starting concentrations on the uptake behaviors of SFR (A) and PO₄³⁻ (B) by HM24 (pH: 5 for PO₄³⁻ and 8 for SFR; a temperature: 30 °C; volume: 100 mL; duration: 24 h; and dose: 0.4 g/L)

3.2.5. Classic isotherm models

Traditional equilibrium analyses for the conducted adsorption processes have been performed in order to evaluate the dispersion of water-soluble pollutants throughout the aqueous solutions alongside the incorporated adsorbent at concentrations higher than the equilibrium level. Conventional equilibrium modeling approaches have a significant impact on illustrating the effective mechanisms. The frequently used isotherm functions provide important insights into three factors: (a) the sorbate's selectivity towards the adsorbent's reactive interfaces; (b) the theoretical amount of soluble chemical ions that could potentially interact with these interfaces; and (c) the maximal adsorption capacities. The present investigation analyzes the equilibrium properties of PO₄³⁻ and SFR by evaluating their bonding aspects using the Langmuir (Fig. 8A and B), Freundlich (Fig. 8C and D), and Dubinin-Radushkevich (D-R) (Fig.8E and F) isotherm theories. The degree of alignment between the assumed equilibrium hypotheses stated in the aforementioned models and the measurable adsorption behaviors of PO₄³⁻ and SFR were evaluated through non-linear regression methods. The analysis included the examination of the correlation coefficient (R²) and the Chi-squared (X²) measurements. The investigation of R² and X² indicates that the HM24 particles tend to adsorb the PO₄³⁻ and SFR ions according to Langmuir's hypothesis rather than the Freundlich concept (Table 2). The mentioned

4<u>5</u>6

53

 equilibrium behavior suggests that PO_4^{3-} and SFR display consistent and homogeneous behaviors during their uptake by reacting sites that are distributed on the interfaces of HM24. As a result, the adsorbed PO_4^{3-} and SFR ions form a single layer or monolayer of their ions on HM24's surface [58, 61]. Furthermore, the analysis showed that HM24 particulates had favorable adsorption behaviors for PO_4^{3-} and SFR, as evidenced by the RL values that are under 1 [18, 51]. The theoretical investigation's results demonstrated that PO_4^{3-} has predicted maximum adsorption capacities (Q_{max}) of 211.4 mg/g at 303 K, 187.5 mg/g at 313 K, and 161.5 mg/g at 323 K. The values for SFR were estimated as follows: 148.1 mg/g at 303 K, 128.6 mg/g at 313 K, and 105.7 mg/g at 323 K (Table 2).

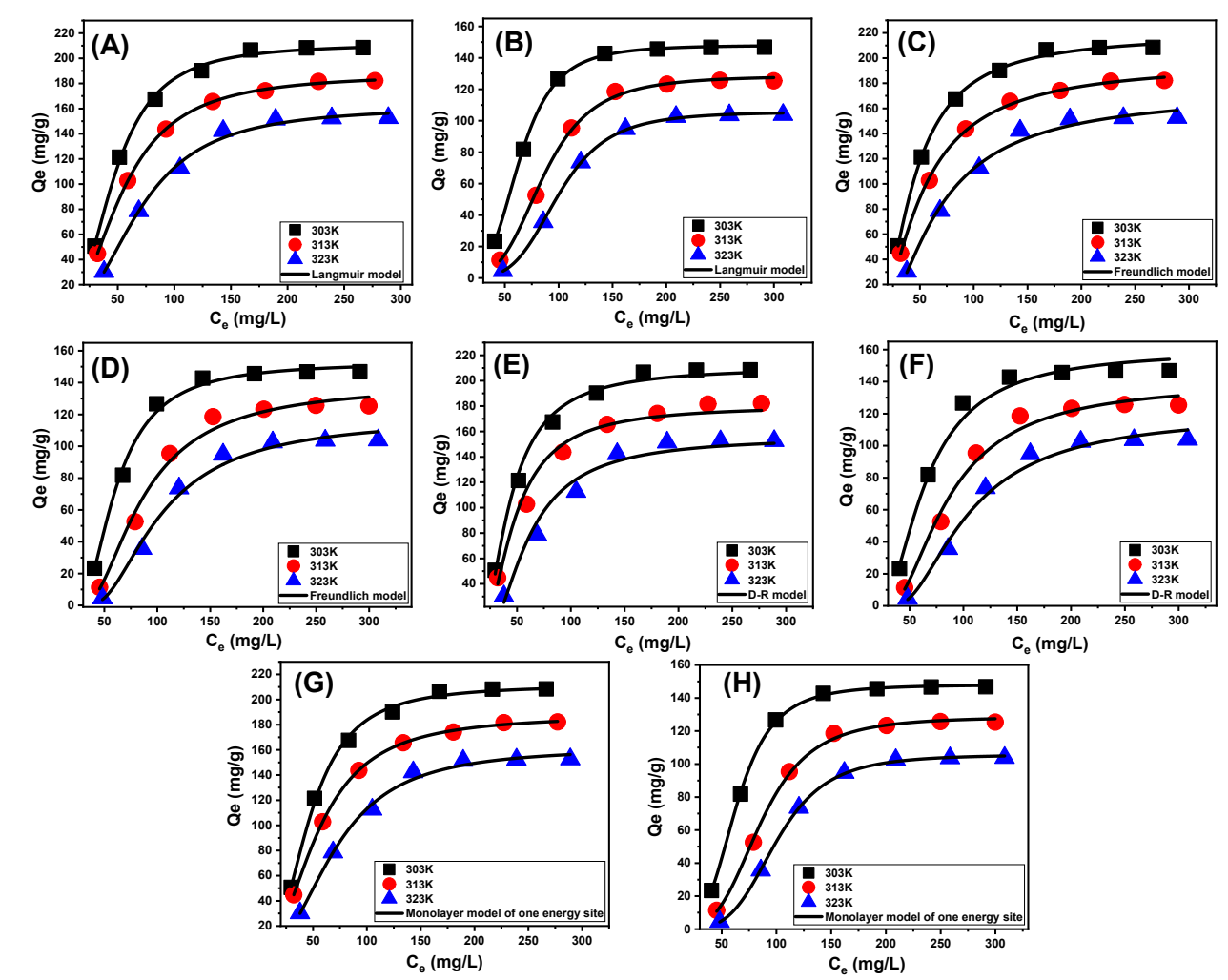


Fig.8. Fitting of the adsorption results by HM24 with Langmuir model (SFR (A) and PO₄³⁻ (B)), Freundlich model (SFR (C) and PO₄³⁻ (D)), D-R model (SFR (E) and PO₄³⁻ (F)), and advanced monolayer model of one energy site (SFR (G) and PO₄³⁻ (H)) (pH: 5 for PO₄³⁻ and 8 for SFR; a temperature: 30 °C; volume: 100 mL; duration: 24 h; and dose: 0.4 g/L)

The equilibrium parameters of the D-R model provide a comprehensive understanding of the energy variations exhibited by HM24 nanoparticles throughout the removal processes of PO₄³⁻ and SFR, irrespective of the particle's levels of heterogeneity or homogeneity. Examining the results of the D-R modeling provides essential details about the free adsorption energy (E) and its significance for understanding the key

4⁴/₆474 4**7**/₈4 4**7**/₉50 4**7**/₉5 52 4**7**/₉6 54 48/₅6 48/₅6 48/₅6 48/₅6 48/₅6 48/₅6

483

mechanisms, whether physical or chemical in nature. The uptake mechanisms may be categorized into three separate groups based on their energetic levels: < 8 kJ/mol, from 8 to 16 kJ/mol, and above 16 kJ/mol. At these energy levels, the main mechanisms comprised mostly of prominent physical, weak chemical, and/or complicated interactions between physical and chemical processes and strong chemical activities in order [55]. The observed values of energy (E) for PO₄³⁻ and SFR uptake processes using HM24 were found to be below the set energy limits for the physical processes (less than 8 kJ/mol) (Table 2).

Table.2. the estimated mathematical parameters of the studied classic equilibrium models (pH: 5 for PO_4^{3-} and 8 for SFR; a temperature: 30 °C; volume: 100 mL; duration: 24 h; and dose: 0.4 g/L)

	Models		303 K	313 K	323 K
			therm models		
SFR		Q _{max} (mg/g)	211.4	187.5	161.5
	Langmuir model	b(L/mg)	6.90 E-5	1.43 E-4	3.77 E-5
		R ²	0.99	0.99	0.99
		X^2	0.07	0.005	0.14
	Freundlich model	1/n	0.77	0.59	0.59
		k _F (mg/g)	218.7	196.8	173.1
		R ²	0.98	0.99	0.99
		X ²	0.13	0.04	0.27
		β (mol²/KJ²)	0.044	0.054	0.107
		Q _m (mg/g)	210.3	180.3	155.5
	D-R model	R ²	0.99	0.98	0.98
		X^2	0.19	0.51	0.73
		E (KJ/mol)	3.4	3.04	2.16
PO ₄ 3-		Q _{max} (mg/g)	148.1	128.6	105.7
	Langmuir model	b(L/mg)	1.39 E-7	5.27 E-8	2.20 E-9
		R ²	0.99	0.99	0.99
		X^2	0.009	0.059	0.010
	Freundlich model	1/n	0.380	0.445	0.435
		k _F (mg/g)	152.4	138.5	117.4
		\mathbb{R}^2	0.98	0.98	0.98
		X ²	0.15	0.47	0.47
		β (mol²/KJ²)	0.012	0.0220	0.032
		Q _m (mg/g)	159.7	139.4	119.6
	D-R model	\mathbb{R}^2	0.99	0.99	0.99
		X ²	0.33	0.38	0.39
		E (KJ/mol)	6.45	4.76	3.95
		Advanced is	otherm model		
SFR	Monolayer model of one energy site	n	2.49	2.22	2.39
		Nm (mg/g)	84.86	84.54	67.44
		Q _{sat} (mg/g)	211.4	187.5	161.5
		C _{1/2} (mg/L)	46.8	54.1	70.2
		ΔE (kJ/mol)	-6.92	-7.52	-8.46
PO ₄ 3-	Monolayer model of one energy site	n	3.81	3.76	4.33
		Nm (mg/g)	38.88	34.14	24.40
		Q _{sat} (mg/g)	148.0	128.6	105.7
		C _{1/2} (mg/L)	63.2	85.7	99.8
		ΔE (kJ/mol)	-4.2	-3.54	-3.25

3.2.6. Advanced isotherm models

The use of statistical physics methods to model the equilibrium characteristics of adsorption reactions could provide a comprehensive examination of these processes' distinctive characteristics. The mathematical models used in the present investigations assess the interactions between external reactive chemical groups that function as interacting binding sites throughout the absorbent's interface and water-soluble pollutants. The mathematical equations utilized in this study provide reliable calculated parameters that precisely reflect the main mechanistic processes, encompassing both energetic and steric factors. The steric parameters included

in the computations are Nm, which quantifies the total quantity of occupied adsorption sites across the

interface of HM24. Furthermore, the calculations include the quantification of the number of chemical ions

adsorbed (n) by just one receptor and the determination of the maximum uptake efficiencies of PO₄3- and SFR

using HM24 when it attains its full saturation (Q_{sat}). The energetic aspects are internal energy (E_{int}), entropy

(Sa), uptake energy (E), and free enthalpy (G). The previously mentioned hypotheses of the established

models have been assessed using non-linear regression analyses. A successful completion of the prior

investigations was achieved by using multivariable nonlinear regression algorithms in conjunction with the

Levenberg-Marquardt iterative approach. Following the obtaining of matching degrees, the adsorption

responses of PO₄3- and SFR by HM24 were evaluated and characterized. The substantially corresponding

model, the monolayer model of a single active site considering the fitting degree (Fig. 8G and H; Table. 2),

was used to complete the assignment. Table 2 displays the calculated variables as fitting parameters for the

4**99** 33 5**00**

35 5**∂**9

37 5**92**

39 503 41

504 43

5<u>44</u>

5<u>46</u>

48

52

5**69** 54

5**⊉6** 56 5**⊉**7

58 5**12**

60

513

5Q3 50 5**9**8

3.2.6.1. Steric properties

used model.

3.2.6.1.1. Number of adsorbed ions per site (n)

The mathematical analysis of the n function provides enough data with regard to the arrangement properties of the immobilized PO₄3- and SFR ions across the exterior surface of HM24. The significance of this includes both the vertical and horizontal arrangements. Moreover, these findings are very significant in understanding the processes that regulate binding reactions, such as multiple dockings or interactions. The uptake of one PO₄3- and SFR ion via multiple uptake sites is significantly affected by the presence of multianchorage or multi-docking processes. As a result, the binding mechanisms have values below 1 and indicate the ions' horizontal positioning. Conversely, behaviors with magnitudes above 1 indicate the existence of PO_4^{3-} and SFR in non-parallel arrangements, in conjunction with a vertical orientation. Multi-ionic actions typically control the removal pathways for such systems, allowing a single site to accommodate several ions [55, 62]. The calculated quantities of n, which indicate the aggregate number of ions bound to a single uptake site onto the exterior of HM24, range from 2.22 to 2.49 for SFR and 3.76 to 4.33 for PO₄³⁻ (Fig. 9A and B). The overall number of PO₄3- and SFR ions adsorbed into each site exceeds 1. Therefore, multi-ionic interacting mechanisms successfully achieved the binding of PO₄3- and SFR. Each single uptake site within the HM24 particulates had the ability to accommodate multiple ions, which were organized in vertical configurations and non-parallel characteristics. Each one of the receptors across the exterior interface of HM24 could effectively accept a maximum of 3 SFR ions and 5 PO₄³- ions. The computed n values of HM24 for PO₄³- and SFR exhibit

a decline as the operating temperature increases from 303 K to 313 K, followed by a further increase as the temperature rises toward 323 K (Fig. 9A and B). These results show that the active chemical groups or adsorption sites change depending on the temperature settings, either becoming active or inactive [62, 63]. Furthermore, conducting the experiments at 323 K significantly improves the aggregation characteristics of PO_4^{3-} and SFR, as evidenced by the rise in their n levels.

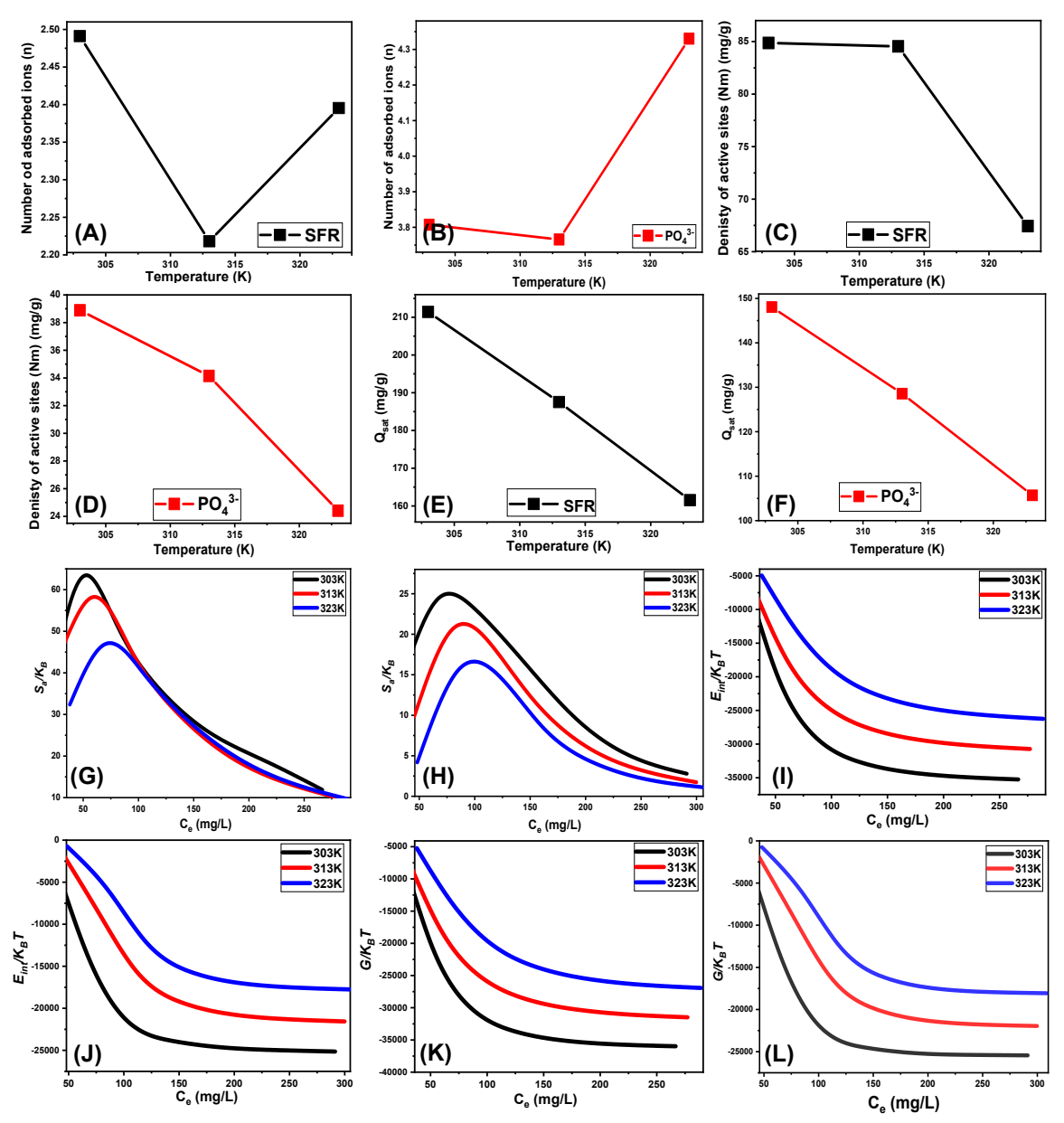


Fig.9. changes in the steric and thermodynamic functions during the uptake of PO_4^{3-} and SFR by HM24 including the number of adsorbed ions per site (SFR (A) and PO_4^{3-} (B)), active sites density (SFR (C) and PO_4^{3-} (D)), saturation adsorption capacity (SFR (E) and PO_4^{3-} (F)), entropy (SFR (G) and PO_4^{3-} (H)), internal energy (SFR (I) and PO_4^{3-} (J)), and enthalpy (SFR (K) and PO_4^{3-} (L)) (pH: 5 for PO_4^{3-} and 8 for SFR; a temperature: 30 °C; volume: 100 mL; duration: 24 h; and dose: 0.4 g/L)

3.2.6.1.2. Density of the active sites (Nm)

A quantitative determination of the overall amount of sites filled with PO_4^{3-} and SFR (Nm) throughout the interactive interfaces of HM24 particulates could potentially be accomplished by assessing the density of the active uptake sites for PO_4^{3-} and SFR (Fig. 9C and D). The values that were determined for Nm at different

565 43 5<u>44</u>

546 547

574

573

temperatures for SFR are 84.86 mg/g at 303 K, 84.5 mg/g at 313 K, and 67.44 mg/g at 323 K (Fig. 9C). The determined values for PO₄³⁻ are 38.88 mg/g at a temperature of 303 K, 34.14 mg/g at 313 K, and 24.4 mg/g at 318 K (Fig. 9D). The observed Nm values corresponding to the adsorption activities of SFR are higher than those that were reported for PO₄³-, thereby elucidating its better adsorption properties. This result provides more evidence for the presence of other chemical groups within the surface of HM24 particles that exhibit an excellent capacity to interact chemically and form complexes with the SFR dye's molecular structure. The Nm values for PO₄3- and SFR exhibit temperature-sensitive reversible variations (Fig. 9C and D). The observed trends are consistent with the estimated variations in n, as the most significant aggregating properties of PO₄3and SFR are observed under elevated temperature conditions, leading to a reduction in the total number of filled sites. Temperature's influence on the activity levels of pre-existing uptake sites could explain the reported behavior [1, 64]. The analysis highlights the negative effects of rising temperatures on the extent of occupied sites, which is illustrated by the deactivation of specific operating sites or the reduction in the duration of time needed for these sites to effectively adsorb and retain PO₄3- and SFR. Previous studies have attributed comparable trends to the assumed diffusion of adsorbed ions or their desorption from the surface of HM24. The reduction in saturation limitations of heated fluids led to the development of the desorption behavior [65].

3.2.6.1.3. Adsorption capacity at the saturation state of (Q_{sat})

The completely saturated adsorption properties of HM24 (Q_{sat}) present the optimal PO₄³⁻ and SFR uptake capacities, together with the highest tolerance levels. The estimated value of Qsat is affected by two primary factors: the designated density of occupied sites (Nm) and the overall number of PO₄3- and SFR ions bound per site (n). HM24 exhibits maximum adsorption capabilities for SFR of 211.4 mg/g at 303 K, 187.5 mg/g at 313 K, and 161.5 mg/g at 323 K (Fig. 9E). The maximum adsorption capacities of PO₄3- were determined to be 148 mg/g at 303 K, 128.6 mg/g at 313 K, and 105.7 mg/g at 323 K (Fig. 9F). The detrimental effects of temperature indicate the exothermic characteristics of the PO₄3- and SFR uptake processes using HM24. These results demonstrate that greater uptake temperatures promote more thermal collisions, which reduces the efficiency of PO₄³⁻ and SFR adsorption [62]. Furthermore, Q_{sat}'s temperature-dependent observable traits show similarities to the behavior characterized by Nm rather than n (Fig. 9E and F). The findings indicate that the total amount of interacting sites, rather than the individual binding value of each individual receptor, is the key factor influencing the efficacy of PO₄³⁻ and SFR adsorption via HM24.

3.2.6.2. Energetic properties

3.2.6.2.1. Adsorption energy

The quantified energy fluctuations (ΔE) during the adsorption processes of PO₄³⁻ and SFR may provide valuable insights into the fundamental mechanisms, regardless of their association with chemical or physical reactions. Physical mechanisms show energies below 40 kJ/mol, whereas chemical pathways reveal energetic levels over 80 kJ/mol. These binding energies serve as a significant criterion for classifying different mechanistic responses of physical processes. The physical interactions presented include hydrogen bonding (energy < 30 kJ/mol), dipole bonding interactions (energy range 2–29 kJ/mol), van der Waals forces (energy range 4–10 kJ/mol), electrostatic attraction (energy range 2–50 kJ/mol), and hydrophobic bonding (energy = 5 kJ/mol). The calculation of the uptake energy levels (ΔE) for PO₄³⁻ and SFR was conducted using Equation 5. This equation employs the solubility PO₄³⁻ and SFR (S), the gas constant (R = 0.008314 kJ/mol·K), the levels of PO₄³⁻ and SFR under half-saturation conditions of HM24, and an established temperature (T) [66].

$$\Delta E = RT \ln \left(\frac{S}{C}\right) \quad (5)$$

For SFR, the adsorption energies range from -6.9 to -8.46 kJ/mol, and for PO_4^{3-} , they range from -3.25 to -4.2 kJ/mol (Table 2). These ranges are within the established limits for physisorption mechanisms. The quantified values for PO_4^{3-} and SFR suggest that hydrogen bonding, electrostatic attraction, dipole interactions, and van der Waals forces are the principal mechanisms facilitating their removal using HM24. The negative values of ΔE indicate that the binding reactions of PO_4^{3-} and SFR by HM24 were exothermic.

3.2.6.2.2. Thermodynamic functions

3.2.6.2.2.1. Entropy

The entropy (Sa) corresponding to the adsorption operations of PO_4^{3-} and SFR employing HM24 clearly illustrates the ordered and disordered properties of their exterior interfaces whenever subjected to different levels of PO_4^{3-} and SFR ions, as well as various temperature conditions. The attributes of Sa were demonstrated by using the results derived from Equation 6, which included the previously determined values for Nm and n, together with the expected levels of PO_4^{3-} and SFR during the half-saturation phases (C1/2).

$$\frac{S_a}{K_B} = Nm \left\{ ln \left(1 + \left(\frac{C}{C_{\frac{1}{2}}} \right)^n \right) - n \left(\frac{C}{C_{\frac{1}{2}}} \right)^n \frac{ln \left(\frac{C}{C_{\frac{1}{2}}} \right)}{1 + \left(\frac{C}{C_{\frac{1}{2}}} \right)^n} \right\}$$
 (6)

The analysis of the resultant graphs reveals a notable decrease in entropy degrees (Sa) upon the adsorption of PO_4^{3-} and SFR utilizing HM24, especially at higher concentrations (Fig. 9G and H). Observations reveal a discernible reduction in the disorder features of HM24 interface when levels of analyzed PO_4^{3-} and SFR increase. The entropy factors additionally reveal the enhancement in the effective docking of PO_4^{3-} and SFR to the vacant and active binding sites situated on the HM24 surface, regardless of low initial

6**219**

26 concentrations [64, 66]. The maximal entropy values for the adsorption of SFR were estimated under equilibrium concentrations of 51.4 mg/L (303 K), 58.8 mg/L (313 K), and 68.5 mg/L (323 K) (Fig. 9G). The equilibrium levels of PO₄³⁻, that correspond to the maximum degree of entropy, were 67.3 mg/L at 303 K, 78.9 mg/L at 313 K, and 85.7 mg/L at 323 K (Fig. 9H). Such equilibrium readings are substantially approximated by the concentrations obtained following the HM24 half-saturation phases. Thus, the existence of leftover binding sites hinders the docking of additional ions. Furthermore, the significant reductions observed in the evaluated entropy levels indicate a substantial decline in the number of available sites, together with a marked drop in the mobility and diffusion properties of the PO₄³⁻ and SFR ions [67].

3.2.6.2.2.2. Internal energy and free enthalpy

The study evaluated the internal energy (E_{int}) associated with the binding interactions of PO_4^{3-} and SFR using HM24, along with the free enthalpy (G), taking into account the variations in PO_4^{3-} and SFR levels, as well as the operational temperatures on these properties. The assessment was performed using Equations 7 and 8, which derived the results based on the predetermined values for Nm, n, and C1/2, together with the translational partition (Zv) [63].

$$\frac{E_{int}}{K_B T} = n N_m \left[\left(\frac{\left(\frac{C}{C_{1/2}} \right)^n ln\left(\frac{C}{Z_v} \right)}{1 + \left(\frac{C}{C_{1/2}} \right)^n} \right) - \left(\frac{n \ln\left(\frac{C}{C_{1/2}} \right) \left(\frac{C}{C_{1/2}} \right)^n}{1 + \left(\frac{C}{C_{1/2}} \right)^n} \right) \right] (7)$$

$$\frac{G}{K_B T} = n N_m \frac{\ln\left(\frac{C}{Z_v} \right)}{1 + \left(\frac{C_{1/2}}{C} \right)^n} (8)$$

The examined fluctuations in E_{int} in terms of the removal process of PO₄³⁻ and SFR using HM24 exhibit negatively signed values. The results showed a significant reduction in E_{int} whenever the temperature increases from 303 K to 323 K (Fig. 9I and J). This investigation confirms the spontaneous and exothermic properties of both ions' adsorption reactions using HM24. The enthalpy assessments and activities display similar characteristics and criteria corresponding to those of the internal energy behaviors. The G data exhibit negative trends and demonstrate a reversible relationship with the specific uptake temperature (Fig. 9K and L). This signifies a decrease in feasibility characteristics and corroborates the exothermic nature and spontaneous features of the adsorption reactions of PO₄³⁻ and SFR ions employing HM24.

3.2.7. Recyclability

The reusing and recycling effectiveness of HM24 as an adsorbent is a critical factor in determining its properties for realistic and large-scale wastewater treatment applications. The leftover HM24 particles, acquired after post-adsorption studies with PO_4^{3-} and SFR, were washed with distilled water for 10 minutes.

The washing procedure was executed four times. The purified HM24 particles were carefully dried inside an electric oven at 50 °C for 8 hours before being used again for subsequent adsorption repeated cycles. The reusable adsorption studies for PO₄3- and SFR were conducted under specified conditions: pH 5 for PO₄3- and pH 8 for SFR, HM24 dosage of 0.4 g/L, content levels of 350 mg/L, contact duration of 24 hours, temperature of 303 K, and a volume of 100 mL (Fig. 10). The outcomes of the five recycling trials reveal the remarkable stability and reusability of HM24 particles for efficient application in removal processes over all five rounds (Fig. 10). The quantities of SFR adsorbed during the analyzed cycles are: 208.5 mg/g (Cycle 1), 208 mg/g (Cycle 2), 205.3 mg/g (Cycle 3), 200.1 mg/g (Cycle 4), 193.7 mg/g (Cycle 5), and 101.5 mg/g (Cycle 6) (Fig. S1). The uptake capacities of PO_4^{3-} were 146.8 mg/g (Cycle 1), 145.5 mg/g (Cycle 2), 140.7 mg/g (Cycle 3), 136.3 mg/g (Cycle 4), 130.8 mg/g (Cycle 5), and 122.3 mg/g (Cycle 6) (Fig. 10). The continuous formation of a complex between the absorbed ions and the chemical structure of hematite could explain the dramatic decrease in the efficacy of HM24 with repeated use. Also detection of the leached iron content demonstrate the high stability of the structure within the studied pH levels, the iron content is less than less than 0.01 mg/L at pH 5 (after the uptake of PO₄³⁻) and below the detection limit at pH 8 (after the uptake of SFR). Such results also signify environmental value of the product within the studied pH range as it will not result in secondary forms of contaminants as byproducts [68, 69].

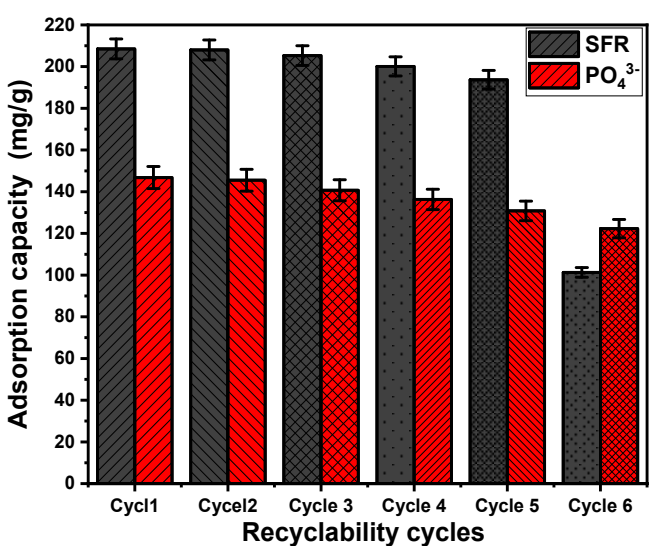


Fig.10. The recyclability properties of HM24 during the uptake of PO_4^{3-} and SFR for six cycles (pH: 5 for PO_4^{3-} and 8 for SFR; a temperature: 30 °C; volume: 100 mL; concentration: 350 mg/L; duration: 24 h; and dose: 0.4 g/L)

3.2.8. Comparison study

The measured adsorption characteristics of HM24 as an adsorbent for PO_4^{3-} and SFR were compared with the recognized results for different types of organic and ion-organic adsorbents. The results indicated the better adsorption qualities of the HM24 compared with the majority of materials listed in Table S2. As a result, the synthetic structure functions well as a cost-effective and environmentally friendly adsorbent for the

6§4

practical treatment of wastewater that contains a variety of soluble organic and inorganic chemical contaminants. The structure is less expensive than the specified adsorbents, and its uses may attain greater removal effectiveness with small dosages and in brief timeframes.

Conclusion:

Well-developed hematite nanorods were simply produced by alkaline modification for natural lateritic iron ore. The obtained rods displayed changes in the exposed crystalline face, mesoporous structure (4.2 nm), and significant surface area (141.5 m 2 /g). The obtained rods were applied as enhanced adsorbents for PO $_4$ ³⁻ and safranin dye (SFR) with uptake capacities of 148 mg/g and 211.4 mg/g, respectively. The results demonstrate that the morphological transformation and associated change in face exposure have a significant effect on the uptake performance of modified hematite compared to natural lateritic iron. The steric results revealed a higher abundance of SFR selective active sites (84.8 mg/g) than PO $_4$ ³⁻ (38.8 mg/g). The phosphate ions tend to aggregate into the interface of hematite with a degree (n = 5) higher than SFR (n = 3), which implies multi-ionic interactions and vertical orientation of the adsorbed ions. The energetic studies and thermodynamic parameters demonstrate the uptake of the two pollutants by spontaneous, physical, and exothermic mechanisms. The simplicity of the synthesis, along with cost considerations, raw material availability, uptake performances, and recyclability, suggests the application of this structure in the practical remediation of agricultural and industrial wastewater.

Acknowledgment:

This publication is funded through the United States Agency for International Development (USAID). The contents are the responsibility of the Authors and do not necessarily reflect the views of USAID or the United States Government. The authors also acknowledge Princess Nourah bint Abdulrahman University Researchers Supporting Project number (PNURSP2024R458), Princess Nourah bint Abdulrahman University, Riyadh, Saudi Arabia.

Data availability statement:

The data will be available up on request to corresponding author

References

6**9**0

6<u>5</u>8 6<u>5</u>9 6**92**

- 1. X. Yang, J. Wang, A.M. El-Sherbeeny, A.A. AlHammadi, W.H. Park, M.R. Abukhadra, Insight into the adsorption and oxidation activity of a ZnO/piezoelectric quartz core-shell for enhanced decontamination of ibuprofen: steric, energetic, and oxidation studies, Chem. Eng. J., 2022, **431**, 134312.
- 2. A. Zourou, A. Ntziouni, N. Adamopoulos, T. Roman, F. Zhang, M. Terrones, K. Kordatos, Graphene oxide-CuFe2O4 nanohybrid material as an adsorbent of Congo red dye, Carbon Trends, 2022, 7, 100147.

7340)

73∳8

732 732

733

734

733 54 736

737

7₹8

7<u>58</u>

- 3. A. Arab, R. El Kurdi, D. Patra, Zinc curcumin oxide nanoparticles for enhanced adsorption of Congo red: kinetics and adsorption isotherms study, Mater. Today Chem., 2022, 23, 100701.
- 4. H. Ighnih, H. Ouachtak, R.E. Malekshah, R. Haounati, A. Jada, A.A. Addi, Synergistic enhancement of pollutant removal from water by using BiOCl/BiOBr heterojunction on clay surface and sunlight irradiation, J. Water Process Eng., 2024, **58**, 104766.
- 5. H.S. Kusuma, N. Illiyanasafa, D.E.C. Jaya, H. Darmokoesoemo, N.R. Putra, Utilization of the microalga Chlorella vulgaris for mercury bioremediation from wastewater and biomass production, Sustain. Chem. Pharm., 2024, 37, 101346.
- 6. J. Wu, Y. Zhong, C. Hao, J. Chen, H. Gao, S. Han, Y. Shen, X. Wang, Emulsion synthesis of cellulose/lanthanum alginate/La(Ⅲ) composite microspheres for efficient and selective adsorption of phosphate, Chem. Eng. J., 2024, 488, 150949.
- 7. M.A. Salam, M. Mokhtar, S.M. Albukhari, D.F. Baamer, L. Palmisano, A.A. AlHammadi, M.R. Abukhadra, Synthesis of zeolite/geopolymer composite for enhanced sequestration of phosphate (PO₄³⁻) and ammonium (NH₄⁺) ions; equilibrium properties and realistic study, J. Environ. Manage., 2021, **300**, 113723.
- 8. S. Tandekar, S. Korde, R.M. Jugade, Red mud-chitosan microspheres for removal of coexistent anions of environmental significance from water bodies, Carbohydr. Polym. Technol. Appl., 2021, **2**, 100128.
- 9. N. Che, J. Qu, J. Wang, N. Liu, C. Li, Y. Liu, Adsorption of phosphate onto agricultural waste biochars with ferrite/manganese modified-ball-milled treatment and its reuse in saline soil, Sci. Total Environ., 2024, **915**, 169841.
- 10. M.G. El-Desouky, A.A. Alayyafi, G.A. Al-Hazmi, A.A. El-Bindary, Effect of metal organic framework alginate aerogel composite sponge on adsorption of tartrazine from aqueous solutions: adsorption models, thermodynamics and optimization via Box-Behnken design, J. Mol. Liq., 2024, 399, 124392.
- 11. Y.A. Neolaka, S.D. Baunsele, F.O. Nitbani, P. de Rozari, B.A. Widyaningrum, Y. Lawa, A.N. Amenaghawon, H. Darmokoesoemo, H.S. Kusuma, Preparation of cellulose adsorbent based on banana peel waste (Musa paradisiaca): Green activation and adsorption of Rhodamine B from the aquatic environment, Nano-Struct. Nano-Objects, 2024, 38, 101146.
- 12. P. Doondani, V. Gomase, D. Saravanan, R.M. Jugade, Chitosan coated cotton-straw-biochar as an admirable adsorbent for reactive red dye, Results Eng., 2022, **15**, 100515.
- 13. I. Ghosh, S. Kar, T. Chatterjee, N. Bar, S.K. Das, Adsorptive removal of Safranin-O dye from aqueous medium using coconut coir and its acid-treated forms: Adsorption study, scale-up design, MPR and GA-ANN modeling, Sustain. Chem. Pharm., 2021, 19, 100374.
- 14. W.A. Shaltout, G.A. El-Naggar, G. Esmail, A.F. Hassan, Synthesis and characterization of ferric@nanocellulose/nanohydroxyapatite bio-composite based on sea scallop shells and cotton stalks: adsorption of Safranin-O dye, Biomass Convers. Biorefin., 2022, 14, 4759–4776.
- 15. C.M.B. De Araujo, G. Wernke, M.G. Ghislandi, A. Diório, M.F. Vieira, R. Bergamasco, M.A. Da Motta Sobrinho, A.E. Rodrigues, Continuous removal of pharmaceutical drug chloroquine and Safranin-O dye from water using agar-graphene oxide hydrogel: Selective adsorption in batch and fixed-bed experiments, Environ. Res., 2023, 216, 114425.
- 16. Y. Jiang, M.R. Abukhadra, N.M. Refay, M.F. Sharaf, M.A. El-Meligy, E.M. Awwad, Synthesis of chitosan/MCM-48 and β-cyclodextrin/MCM-48 composites as bio-adsorbents for environmental removal of Cd²⁺ ions; kinetic and equilibrium studies, React. Funct. Polym., 2020, **154**, 104675.
- 17. A.M. Alsuhaibani, A.A. Alayyafi, L.A. Albedair, M.G. El-Desouky, A.A. El-Bindary, Synthesis and characterization of metal—organic frameworks based on thorium for the effective removal of 2,4-dichlorophenylacetic pesticide from water: batch adsorption and Box-Behnken Design optimization, and evaluation of reusability, J. Mol. Liq., 2024, 398, 124252.
- 18. K. Wu, C. Tao, C. Zhang, Z. Hao, A. Li, C. Duan, T. Liu, Z. Li, Fabrication of double-shell CuOx@Fe3O4 hollow spheres for efficient adsorption removal of tetracycline and oxytetracycline from water, J. Water Process Eng., 2023, **56**, 10438.
- 19. A.M. Alsuhaibani, A.A. Alayyafi, L.A. Albedair, M.G. El-Desouky, A.A. El-Bindary, Efficient fabrication of a composite sponge for Cr(VI) removal via citric acid cross-linking of metal-organic framework and chitosan: adsorption isotherm, kinetic studies, and optimization using Box-Behnken design, Mater. Today Sustain., 2024, 26, 100732.
- 20. S.M. Albukhari, M.A. Salam, M.R. Abukhadra, Effective retention of inorganic Selenium ions (Se(VI) and Se(IV)) using novel sodalite structures from muscovite; characterization and mechanism, J. Taiwan Inst. Chem. Eng., 2021, **120**, 116-126.
- 21. V. Gomase, T. Rathi, D. Saravanan, R. Jugade, Amputation of Remazol brilliant blue dye on crosslinked chitosan hydrogel: Statistical treatment and experimental evaluation, Environ. Res., 2024, **252**, 118764.

747

74/8

749

75<u>0</u> 753

752 75

753

75*4*

798

756 758

757

738

759 24

769

7016

782

763 763

764

7**6**5

766 766

767

768

769

73g

7739

7#2

7/33 7/43

7743

7745

776 46

7747

7**7**48

719

7<u>8</u>0

78≴

782

784

784

785

788

7&7

- 22. M.R. Abukhadra, M.G. Basyouny, A.M. El-Sherbeeny, M.A. El-Meligy, The effect of different green alkali modification processes on the clinoptilolite surface as adsorbent for ammonium ions; characterization and application, Microporous Mesoporous Mater., 2020, 300, 110145.
- 744 23. R. EL Kaim Billah, A. Zaghloul, H.A. Ahsaine, A. BaQais, I. Khadoudi, N. El Messaoudi, M. Agunaou, A. Soufiane, R. Jugade,
 Methyl orange adsorption studies on glutaraldehyde cross-linking chitosan/fluorapatite-based natural phosphate composite, Int. J.
 Environ. Anal. Chem., 2022, 1-17.
 - 24. X. Sun, N. Talha, A.M. Ahmed, M.A. Rafea, N.A. Alenazi, M.R. Abukhadra, Steric and energetic studies on the influence of cellulose on the adsorption effectiveness of Mg trapped hydroxyapatite for enhanced remediation of chlorpyrifos and omethoate pesticides, Int. J. Biol. Macromol., 2024, 265, 130711.
 - 25. Y. Chen, M. Li, Y. Liu, Y. Liu, Y. Chen, H. Li, L. Li, F. Xu, H. Jiang, L. Chen, Hydroxyapatite modified sludge-based biochar for the adsorption of Cu2+ and Cd2+: adsorption behavior and mechanisms, Bioresour. Technol., 2021, 321, 124413.
 - 26. W. Chen, G. Guo, L. Huang, L. Ouyang, Q. Shuai, Facet-dependent adsorption of aromatic organoarsenicals on hematite: The mechanism and environmental impact, J. Hazard. Mater., 2024, **464**, 132976.
 - 27. Z. Tao, Q. Zhou, T. Zheng, F. Mo, S. Ouyang, Iron oxide nanoparticles in the soil environment: Adsorption, transformation, and environmental risk, J. Hazard. Mater., 2023, **459**, 132107.
 - 28. C.A. Mbachu, A.K. Babayemi, T.C. Egbosiuba, J.I. Ike, I.J. Ani, S. Mustapha, Green synthesis of iron oxide nanoparticles by Taguchi design of experiment method for effective adsorption of methylene blue and methyl orange from textile wastewater, Results Eng., 2023, 19, 101198.
 - 29. B.E. Keshta, A.H. Gemeay, D.K. Sinha, S. Elsharkawy, F. Hassan, N. Rai, C. Arora, State of the art on the magnetic iron oxide Nanoparticles: Synthesis, Functionalization, and applications in wastewater treatment, Results Chem., 2024, 101388.
 - 30. J. Talibawo, P.I. Kyesmen, M.C. Cyulinyana, M. Diale, Facile Zn and Ni Co-Doped Hematite Nanorods for Efficient Photocatalytic Water Oxidation, Nanomaterials, 2022, **12**, 2961.
 - 31. Y. Dehmani, A.A. Alrashdi, H. Lgaz, T. Lamhasni, S. Abouarnadasse, I.-M. Chung, Removal of phenol from aqueous solution by adsorption onto hematite (α-Fe2O3): Mechanism exploration from both experimental and theoretical studies, Arabian J. Chem., 2020, 13, 5474–5486.
 - 32. S. Rajendran, S.G. Wanale, A. Gacem, V.K. Yadav, I.A. Ahmed, J.S. Algethami, S.D. Kakodiya, T. Modi, A.M. Alsuhaibani, K.K. Yadav, S. Cavalu, Nanostructured Iron Oxides: Structural, Optical, Magnetic, and Adsorption Characteristics for Cleaning Industrial Effluents, Crystals, 2023, 13, 472.
 - 33. A. Gulzar, N. Ayoub, J.F. Mir, A.M. Alanazi, M.A. Shah, A. Gulzar, In vitro and in vivo MRI imaging and photothermal therapeutic properties of Hematite (α-Fe2O3) Nanorods, J. Mater. Sci. Mater. Med., 2022. https://doi.org/10.1007/s10856-021-06636-1.
 - 34. Z. Li, J. Wu, L. Liao, X. He, B. Huang, S. Zhang, Y. Wei, S. Wang, W. Zhou, Surface engineering of hematite nanorods photoanode towards optimized photoelectrochemical water splitting, J. Colloid Interface Sci., 2022, 626, 879–888.
 - 35. D.H. Kim, T.H. Kim, W. Sohn, J.M. Suh, Y.-S. Shim, K.C. Kwon, K. Hong, S. Choi, H.-G. Byun, J.-H. Lee, H.W. Jang, Au decoration of vertical hematite nanotube arrays for further selective detection of acetone in exhaled breath, Sens. Actuators B Chem., 2018, 274, 587–594.
 - 36. W. Wang, W. Zhang, Y. Fan, C. Qu, W. Ren, X. Huang, M. Hong, F. Liu, H. Yin, Facet-dependent adsorption of aluminum(III) on hematite nanocrystals and the influence on mineral transformation, Environ. Sci. Nano, 2022, **9**, 2073–2085.
 - 37. D.M.S.N. Dissanayake, M.M.M.G.P.G. Mantilaka, T.C. Palihawadana, G.T.D. Chandrakumara, R.T. De Silva, H.M.T.G.A. Pitawala, K.M.N. De Silva, G.A.J. Amaratunga, Facile and low-cost synthesis of pure hematite (α-Fe2O3) nanoparticles from naturally occurring laterites and their superior adsorption capability towards acid-dyes, RSC Adv., 2019, 9, 21249–21257.
 - 38. T. Tatarchuk, A. Shyichuk, N. Danyliuk, I. Lapchuk, W. Macyk, Water disinfection using hydrogen peroxide with fixed bed hematite catalyst kinetic and activity studies, Environ. Sci. Pollut. Res., 2024, 31, 26592–26605.
 - 39. N. Khorshidi, A.R. Azadmehr, Competitive adsorption of Cd(II) and Pb(II) ions from aqueous solution onto Iranian hematite (Sangan mine): Optimum condition and adsorption isotherm study, Desalination Water Treat., 2017, **58**, 106–119.
 - 40. S. Bai, J. Li, Y. Bi, J. Yuan, S. Wen, Z. Ding, Adsorption of sodium oleate at the microfine hematite/aqueous solution interface and its consequences for flotation, Int. J. Min. Sci. Technol., 2023, **33**, 105–113.
 - 41. H. Xie, S. Zhang, L. Zhong, Q. Wang, J. Hu, A. Tang, Effect of the occurrence state of magnesium in talc on the adsorption of Pb(II), J. Alloys Compd., 2021, 887, 161288.

- 7**9**-2 793
- 794 795
- 796 797 798 799
- 8ģģ 893 80**2** 803
- 804 804 805 8**9**8 807
- 898 8**09** 810 8<u>1</u>1
- 813 8⊉3 833 835
- 8**1**6 819 818 8**139**
- 8210 821 821 8**4**3 8**213** 8**2**4 46
- 8**246** 829 8<u>5</u>8 8**39**

- 8**≸**₿ 834 833
- 834 59 835 836

- 42. H. Fu, Y. Yang, R. Zhu, J. Liu, M. Usman, Q. Chen, H. He, Superior adsorption of phosphate by ferrihydrite-coated and lanthanum-decorated magnetite, J. Colloid Interface Sci., 2018, 530, 704-713.
- 43. A.M. Saad, M.R. Abukhadra, S.A.-K. Ahmed, A.M. Elzanaty, A.H. Mady, M.A. Betiha, J.-J. Shim, A.M. Rabie, Photocatalytic degradation of malachite green dye using chitosan supported ZnO and Ce-ZnO nano-flowers under visible light, J. Environ. Manage., 2020, 258, 110043.
- 44. Y. Bruneel, L. Van Laer, S. Brassinnes, E. Smolders, Characterisation of the highly selective caesium sorption on glauconite rich sands of contrasting geological formations, Appl. Geochem., 2021, 128, 104926.
- 45. M.R. Abukhadra, M. Mostafa, Effective decontamination of phosphate and ammonium utilizing novel muscovite/phillipsite composite; equilibrium investigation and realistic application, Sci. Total Environ., 2019, 667, 101-111.
- 46. Y.A.B. Neolaka, G. Supriyanto, H. Darmokoesoemo, H.S. Kusuma, Characterization, kinetic, and isotherm data for Cr(VI) removal from aqueous solution by Cr(VI)-imprinted poly(4-VP-co-MMA) supported on activated Indonesia (Ende-Flores) natural zeolite structure, Data Brief, 2018, 17, 969-979.
- 47. Y.A.B. Neolaka, Y. Lawa, J. Naat, A.A.P. Riwu, Y.E. Lindu, H. Darmokoesoemo, B.A. Widyaningrum, M. Iqbal, H.S. Kusuma, Evaluation of magnetic material IIP@GO-Fe3O4 based on Kesambi wood (Schleichera oleosa) as a potential adsorbent for the removal of Cr(VI) from aqueous solutions, React. Funct. Polym., 2021, 166, 105000.
- 48. Y.A.B. Neolaka, Y. Lawa, J. Naat, A.A.P. Riwu, A.W. Mango, H. Darmokoesoemo, B.A. Widyaningrum, M. Iqbal, H.S. Kusuma, Efficiency of activated natural zeolite-based magnetic composite (ANZ-Fe3O4) as a novel adsorbent for removal of Cr(VI) from wastewater, J. Mater. Res. Technol., 2022, 18, 2896-2909.
- 49. A.M. El-Sherbeeny, S.M. Ibrahim, A.A. AlHammadi, A.T.A. Soliman, J.J. Shim, M.R. Abukhadra, Effective retention of radioactive Cs+ and Ba2+ ions using β -cyclodextrin functionalized diatomite (β -CD/D) as environmental adsorbent; characterization, application, and safety, Surf. Interfaces, 2021, 26, 101434.
- 50. M. Abdel Salam, M. Mokhtar, S.M. Albukhari, D.F. Baamer, L. Palmisano, M. Jaremko, M.R. Abukhadra, Synthesis and Characterization of Green ZnO@polynaniline/Bentonite Tripartite Structure (G.Zn@PN/BE) as Adsorbent for As(V) Ions: Integration, Steric, and Energetic Properties, Polymers, 2022, 14(12), 2329.
- 51. E. El Qada, Kinetic Behavior of the Adsorption of Malachite Green Using Jordanian Diatomite as Adsorbent, Jordan J. Eng. Chem. Ind., 2020, 3(1).
- 52. X. Lin, Y. Xie, H. Lu, Y. Xin, R. Altaf, S. Zhu, D. Liu, Facile preparation of dual La-Zr modified magnetite adsorbents for efficient and selective phosphorus recovery, Chem. Eng. J., 2021, 413, 127530.
- 53. Y.A.B. Neolaka, G. Supriyanto, H. Darmokoesoemo, H.S. Kusuma, Characterization, kinetic, and isotherm data for Cr(VI) removal from aqueous solution by Cr(VI)-imprinted poly(4-VP-co-MMA) supported on activated Indonesia (Ende-Flores) natural zeolite structure, Data Brief, 2018, 17, 969-979.
- 54. M.A. Salam, M.R. Abukhadra, M. Mostafa, Effective decontamination of As(V), Hg(II), and U(VI) toxic ions from water using novel muscovite/zeolite aluminosilicate composite: adsorption behavior and mechanism, Environ. Sci. Pollut. Res., 2020, 27(12), 13247– 13260.
- 55. I.R. Sayed, A.M. Farhan, A.A. AlHammadi, M.I. El-Sayed, I.M. Abd El-Gaied, A.M. El-Sherbeeny, W. Al Zoubi, Y.G. Ko, M.R. Abukhadra, Synthesis of novel nanoporous zinc phosphate/hydroxyapatite nano-rods (ZPh/HPANRs) core/shell for enhanced adsorption of Ni2+ and Co2+ ions: Characterization and application, J. Mol. Lig., 2022, 360, 119527.
- 56. Y.A.B. Neolaka, A.A.P. Riwu, U.O. Aigbe, K.E. Ukhurebor, R.B. Onyancha, H. Darmokoesoemo, H.S. Kusuma, Potential of activated carbon from various sources as a low-cost adsorbent to remove heavy metals and synthetic dyes, Results Chem., 2023, **5,** 100711.
- 57. H.M. Nassef, G.A. Al-Hazmi, A.A. Alayyafi, M.G. El-Desouky, A.A. El-Bindary, Synthesis and characterization of new composite sponge combining of metal-organic framework and chitosan for the elimination of Pb(II), Cu(II) and Cd(II) ions from aqueous solutions: Batch adsorption and optimization using Box-Behnken design, J. Mol. Liq., 2024, 394, 123741.
- 58. A. Almahri, M. Morad, M.M. Aljohani, N.M. Alatawi, F.A. Saad, H.M. Abumelha, M.G. El-Desouky, A.A. El-Bindary, Atrazine reclamation from an aqueous environment using a ruthenium-based metal-organic framework, Process Saf. Environ. Prot., 2023, 177, 52-68.
- 59. E.E. Jasper, V.O. Ajibola, J.C. Onwuka, Nonlinear regression analysis of the sorption of crystal violet and methylene blue from aqueous solutions onto an agro-waste derived activated carbon, Appl. Water Sci., 2020, 10(6), 1-11.

- 60. A.M. Ahmed, I. Saad, M.A. Rafea, M.R. Abukhadra, Synergetic and advanced isotherm investigation for the enhancement influence of zeolitization and β-cyclodextrin hybridization on the retention efficiency of U(vi) ions by diatomite, RSC Adv., 2024, **14**, 8752–8768.
- 61. F. Dawodu, G. Akpomie, M. Abuh, Equilibrium Isotherm Studies on the Batch Sorption of Copper (II) ions from Aqueous Solution unto Nsu Clay, Int. J. Sci. Eng. Res., 2012, **3(12)**, 1-7.
- 62. M. Mobarak, R.A. Ali, M.K. Seliem, Chitosan/activated coal composite as an effective adsorbent for Mn(VII): Modeling and interpretation of physicochemical parameters, Int. J. Biol. Macromol., 2021, 186, 750-758.
- 63. F. Dhaouadi, L. Sellaoui, H.E. Reynel-Ávila, V. Landín-Sandoval, D.I. Mendoza-Castillo, J.E. Jaime-Leal, E.C. Lima, A. Bonilla-Petriciolet, A.B. Lamine, Adsorption mechanism of Zn²⁺, Ni²⁺, Cd²⁺, and Cu²⁺ ions by carbon-based adsorbents: interpretation of the adsorption isotherms via physical modeling, Environ. Sci. Pollut. Res., 2021, **28**, 30943–30954.
- 64. L. Sellaoui, J. Ali, M. Badawi, A. Bonilla-Petriciolet, Z. Chen, Understanding the adsorption mechanism of Ag+ and Hg2+ on functionalized layered double hydroxide via statistical physics modeling, Appl. Clay Sci., 2020, 198, 105828.
- 65. A.M. Ahmed, N. Nasser, M.A. Rafea, M.R. Abukhadra, Effective retention of cesium ions from aqueous environment using morphologically modified kaolinite nanostructures: experimental and theoretical studies, RSC Adv., 2024, **14**, 3104–3121.
- 66. F. Dhaouadi, L. Sellaoui, M. Badawi, H.E. Reynel-Ávila, D.I. Mendoza-Castillo, J.E. Jaime-Leal, A. Bonilla-Petriciolet, A.B. Lamine, Statistical physics interpretation of the adsorption mechanism of Pb²⁺, Cd²⁺ and Ni²⁺ on chicken feathers, J. Mol. Liq., 2020, **319**, 114168.
- 67. L. Sellaoui, H. Guedidi, L. Reinert, S. Knani, L. Duclaux, A.B. Lamine, Experimental and theoretical studies of adsorption of ibuprofen on raw and two chemically modified activated carbons: new physicochemical interpretations, RSC Adv., 2016, 6(15), 12363-12373.
- 68. A. Shekhawat, R. Jugade, S. Kahu, D. Saravanan, S. Deshmukh, Mesoporous cellulose assemblage Al-doped ferrite for sustainable defluoridation process based on parameters optimization through RSM, Inorg. Chem. Commun., 2023, **151,** 110528.
- 69. S. Korde, S. Tandekar, R.M. Jugade, Novel mesoporous chitosan-zirconia-ferrosoferric oxide as magnetic composite for defluoridation of water, J. Environ. Chem. Eng., 2020, **8**(5), 104360.

All the presented data in the study will be available up on reasonable request to corresponding author